remote sensing

MDPI

Article

Pre-, Co-, and Post-Failure Deformation Analysis of the Catastrophic Xinjing Open-Pit Coal Mine Landslide, China, from Optical and Radar Remote Sensing Observations

Fengnian Chang †, Houyu Li †, Shaochun Dong * and Hongwei Yin

School of Earth Sciences and Engineering, Nanjing University, Nanjing 210023, China; cfn@smail.nju.edu.cn (F.C.); houyuli@smail.nju.edu.cn (H.L.); hwyin@nju.edu.cn (H.Y.)

* Correspondence: dsc@nju.edu.cn

† These authors contribute equally to this work.

Abstract: Landslide risks in open-pit mine areas are heightened by artificial slope modifications necessary for mining operations, endangering human life and property. On 22 February 2023, a catastrophic landslide occurred at the Xinjing Open-Pit Coal Mine in Inner Mongolia, China, resulting in 53 fatalities and economic losses totaling 28.7 million USD. Investigating the pre-, co-, and post-failure deformation processes and exploring the potential driving mechanisms are crucial to preventing similar tragedies. In this study, we used multi-source optical and radar images alongside satellite geodetic methods to analyze the event. The results revealed pre-failure acceleration at the slope toe, large-scale southward displacement during collapse, and ongoing deformation across the mine area due to mining operations and waste accumulation. The collapse was primarily triggered by an excessively steep, non-compliant artificial slope design and continuous excavation at the slope's base. Furthermore, our experiments indicated that the commonly used Sentinel-1 Interferometric Synthetic Aperture Radar (InSAR) significantly underestimated landslide deformation due to the maximum detectable deformation gradient (MDDG) limitation. In contrast, the high-spatial-resolution Fucheng-1 provided more accurate monitoring results with a higher MDDG. This underscores the importance of carefully assessing the MDDG when employing InSAR techniques to monitor rapid deformation in mining areas.

Keywords: open-pit coal mine landslide; deformation analysis; InSAR; Fucheng-1; Sentinel-1

check for updates

Academic Editors: Mingsheng Liao, Wenyu Gong, Jie Dong, Liming Jiang, Menghua Li and Xinjian Shan

Received: 24 November 2024
Revised: 18 December 2024
Accepted: 23 December 2024
Published: 25 December 2024

Citation: Chang, F.; Li, H.; Dong, S.; Yin, H. Pre-, Co-, and Post-Failure Deformation Analysis of the Catastrophic Xinjing Open-Pit Coal Mine Landslide, China, from Optical and Radar Remote Sensing Observations. *Remote Sens.* **2025**, *17*, 19. https://doi.org/10.3390/rs17010019

Copyright: © 2024 by the authors. Licensee MDPI, Basel, Switzerland. This article is an open access article distributed under the terms and conditions of the Creative Commons Attribution (CC BY) license (https://creativecommons.org/licenses/by/4.0/).

1. Introduction

Coal is an essential energy source, and open-pit mining is widely practiced globally due to its simplicity and cost-effectiveness [1–3]. However, with continued mining operations, the risk of geohazards escalates due to engineering disturbances, particularly in the form of landslides and collapses [4]. On 22 February 2023, at 13:12 (UTC+8), a catastrophic landslide struck the Xinjing Open-Pit Coal Mine in Alxa Left Banner, Inner Mongolia, China, burying numerous miners and vehicles in operation [2,4–6]. Later that day, at 18:44, a secondary collapse occurred at the same site, further complicating rescue efforts [2,4]. Despite the extensive efforts of local authorities, the disaster tragically claimed 53 lives [5].

A proactive approach to prevent such disasters involves real-time monitoring of mining areas to detect landslide precursors [7,8]. Similar efforts include using in situ equipment like GNSS, total stations, and slope radar for artificial slope monitoring [9,10]. However, due to constraints in monitoring range, costs, and the unexpected nature of this event, high-precision monitoring devices were not installed in the collapse zone beforehand.

A remote sensing technique presents a viable alternative, offering high efficiency, precision, wide coverage, and economic benefits for monitoring open-pit mine collapse [1,2,11].

Remote-sensing-based surface deformation monitoring primarily relies on Interferometric Synthetic Aperture Radar (InSAR) and its advanced methods, including Differential InSAR (D-InSAR) [12], Permanent Scatterer InSAR (PS-InSAR) [13–16], and Small BAseline Subset InSAR (SBAS-InSAR) [17,18]. These methods can deliver deformation monitoring accuracy at the centimeter to millimeter level; however, they are limited by monitoring dimensions, decorrelation, atmospheric effects, and satellite revisit cycles [19,20]. Moreover, InSAR technology is suitable only for detecting slow-moving landslides (with deformations from centimeters to meters annually) and is inadequate for monitoring large-magnitude, co-failure deformation during landslide collapse [20]. In contrast, optical remote sensing offers high-resolution (sub-meter to meter level) imagery for direct interpretation and delineation of landslide collapse areas, aiding in rescue efforts [1,2]. Additionally, Pixel Offset Tracking (POT) based on optical images can reconstruct large-scale horizontal deformation (meters to kilometers) [21,22], providing complementary information to InSAR. However, the precision of this approach depends on image resolution (~1/10 of resolution), making it less effective for small-magnitude deformations [23,24].

Relevant scholars have conducted extensive research on the Xinjing landslide accident using remote sensing data, crowdsourced information, seismic signals, and various analytical methods, including InSAR, particle image velocimetry (PIV), photogrammetric techniques, and seismic inversion analyses [1,2,4,6,25,26]. Zhang et al. [1], An et al. [2], and Wu et al. [26] employed Sentinel-1 and Radarsat-2 SAR data to capture the spatiotemporal deformation of the landslide before the collapse. An et al. [25] utilized crowdsourced data to examine the landslide's size, movement direction, and speed at the time of occurrence. Wang et al. [4] applied seismic data to invert for volume, velocity, and horizontal displacement during the collapse. Li et al. [6] conducted a retrospective analysis of the event using PIV and remote sensing methods. However, these studies each focused on specific stages of landslide deformation, lacking a comprehensive investigation covering the entire deformation processes.

In this study, we utilized multi-source SAR and optical imagery to comprehensively analyze the full-process deformation of the Xinjing landslide, covering the pre-, co-, and post-failure phases. Specifically, we monitored pre- and post-event deformations across the entire mining area using InSAR, while co-failure horizontal displacements were inverted from high-resolution optical imagery through the POT method. Additionally, we employed high-resolution SAR images to reconstruct the post-event Digital Elevation Model (DEM) of the mining area to assess vertical deformation. Finally, we investigated the causative mechanisms behind the landslide collapse in the mining area based on these monitoring results.

2. Background of the Xinjing Landslide

The Xinjing Open-Pit Coal Mine, located in Alxa Left Banner, Inner Mongolia Autonomous Region, China (Figure 1a,b), is positioned on the southern side of Helan Mountain, an area marked by complex geology shaped by ancient aulacogen deposition and subsequent tectonic processes, including fault reactivation and uplift folding [4,27]. This geologic background has led to intricate stratigraphic formations and structural weaknesses with numerous faults and folds [4]. Mining operations are focused on two large opposing open-pit slopes oriented north–south at the center of the site, surrounded by mining dumps (Figure 1c). The mine, a concave pit reaching depths of up to 180 m, primarily extracts coal from the Jurassic Yan'an Formation ($J_{1–2y}$) [4], known for its rich coal seams. Its stratigraphy

features a monoclinic structure with a strike of approximately 295° and a dip ranging from 10° to 20° [5,6].

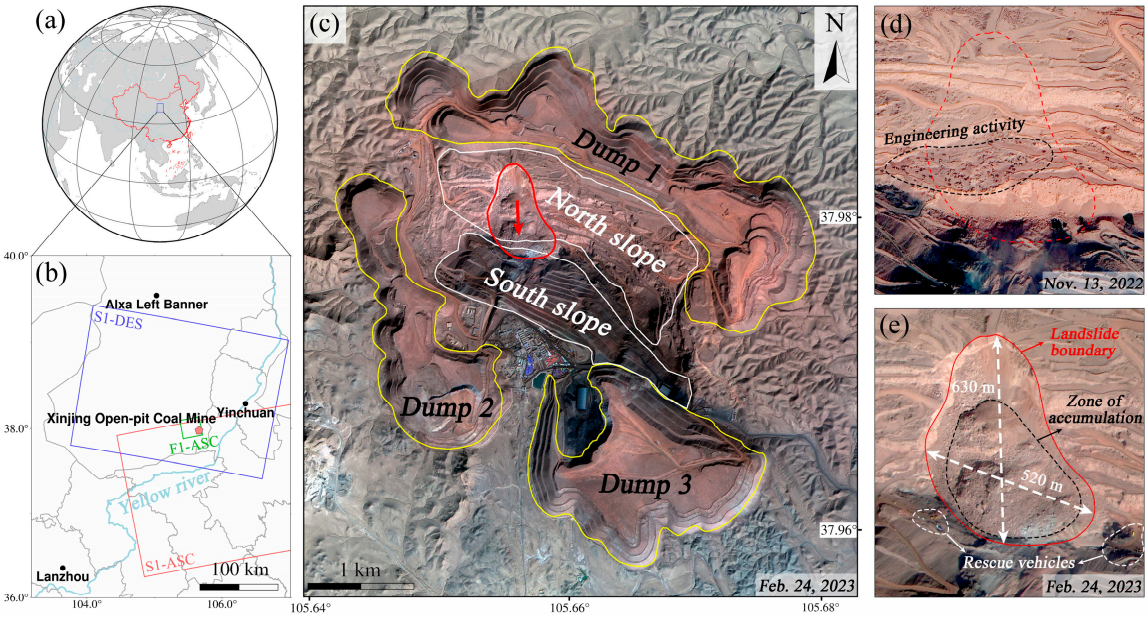

Figure 1. Overview map of the study area. (**a**,**b**) illustrate the location of the Xinjing open-pit coal mine, with boxes in (**b**) representing the footprints of Sentinel-1 ascending (S1-ASC), Sentinel-1 descending (S1-DES), and Fucheng-1 ascending tracks (F1-ASC); (**c**) is the coverage of the mine and collapse area provided by the GF-2 satellite image, where the red arrow indicates the direction of collapse; (**d**,**e**) are GF-2 optical images of the landslide area before and after the collapse, respectively.

On 22 February 2023, at 13:12 local time (UTC+8), a catastrophic landslide occurred on the north slope of the Xinjing mine (Figure 1c), leading to severe consequences [1,5]. The landslide, initiated at the slope toe, triggered a rapid downward movement of rock and debris, forming a large fan-shaped deposit (Figure 1c,e) that engulfed miners and equipment below. A secondary collapse later that day intensified the rescue challenges. This tragic event resulted in 53 fatalities, six injuries, and estimated economic losses of 28.7 million USD [5].

3. Data and Methods

3.1. Multi-Source Remote Sensing Data

Launched in 2014 under the European Space Agency's Copernicus Mission, the Sentinel-1A satellite is equipped with a C-band SAR system. Benefiting from the open access data policy, Sentinel-1 has become one of the most widely used datasets in the InSAR community due to its global coverage and systematic acquisition strategy. The Fucheng-1 satellite, launched in 2023 by Spacety Co., Ltd. in Changsha, China, is a C-band commercial lightweight SAR satellite designed for precise deformation monitoring of small areas with higher spatial resolution [28,29]. In Spotlight (SP) mode, its ground resolution reaches less than 1 m, and in Stripmap (SM) mode, it is approximately 1.5 m (Table 1). The interferometric revisit interval for Fucheng-1 is 11 days [29], comparable to the 12-day revisit interval of a single Sentinel-1 satellite.

Table 1. Basic parameters of SAR data used for InSAR analysis.

Stage	SAR Platform	Mode	Orbit	Pixel Spacing (Rg × Az) (m)	Incidence Angle (°)	Critical Baseline (m)	Time Span *	Images	Image Pairs
Pre-failure	Sentinel-1	IW	Ascending	2.33 × 13.91	37.7	5044	20200106–20221115	74	229
	Sentinel-1	IW	Descending	2.33 × 13.93	36.9	5688	20200111–20210529	43	153
Post-failure	Sentinel-1	IW	Ascending	2.33 × 13.91	37.7	5043	20230408–20240309	9	23
	Fucheng-1	SM	Ascending	0.62 × 1.57	31.0	11,572	20240104–20240526	13	49

* The date format is "yyyymmdd".

To systematically review the deformation and causes of the Xinjing coal mine landslide, we collected multi-source remote sensing data, including all available ascending (Path 157, Frame 117) and descending (Path 62, Frame 464–466) Sentinel-1 SAR data from January 2020 to March 2024, and ascending Fucheng-1 SAR data from January 2024 to May 2024 (Table 1). Given that the deformation magnitude of the landslide collapse (hundreds of meters, based on [5]) far exceeds the monitoring capabilities of InSAR, we divided the SAR data into four groups based on the event date (Table 1, Figure 2a). Furthermore, high-resolution optical images from GaoFen-2 (GF-2) and PlanetScope [30] were obtained pre- and post-event (Table 2) to delineate landslide boundaries and aid in analyzing the causes of surface deformation. Shuttle Radar Topography Mission (SRTM) and Copernicus (COP) digital elevation models (DEMs) were employed to reconstruct the elevation history of the mining area (Figure 2b and Table 3), with ICESat-2 terrain elevation data used for validation [31].

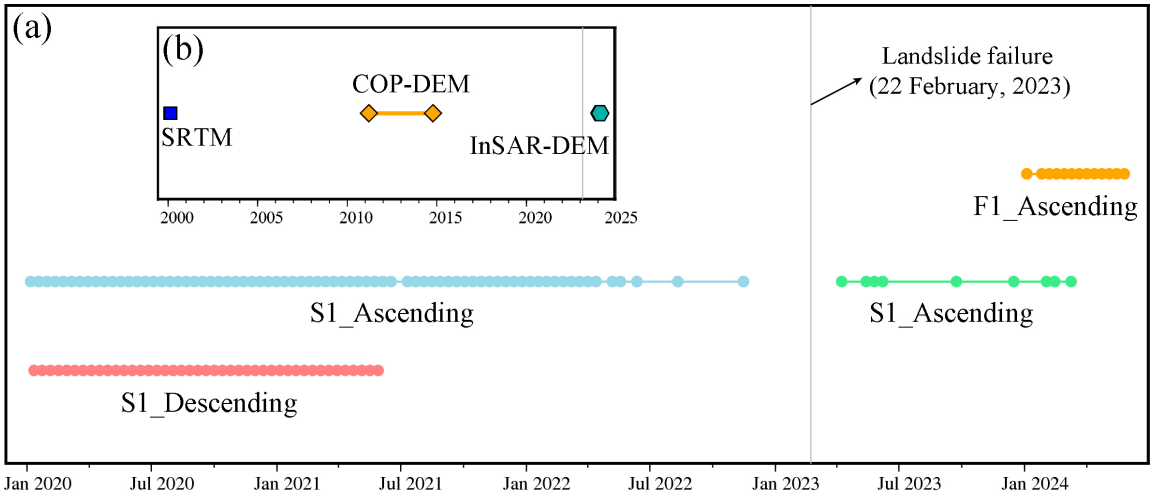

Figure 2. Time spans covered by (**a**) four sets of SAR data and (**b**) DEMs used in this study.

Table 2. Basic parameters of optical images used for this study.

Satellite Platform	Pixel Spacing (m)	Product Type	Imaging Date *	Sensor
GaoFen-2	0.8 × 0.8	L1A	20221113, 20230224	PMS1
PlanetScope	3 × 3	L3B	20230222, 20230224	PSB.SD

* The date format is "yyyymmdd".

Table 3. Basic parameters of DEMs used in this study.

Product	Resolution (m)	Elevation Measurement Accuracy (LE90) (m)	Planar Measurement Accuracy (CE90) (m)	Imaging Date *
SRTM-DEM	30	16	20	2000
COP-DEM	30	4	6	2011–2015

* The date format is "yyyy".

3.2. SBAS InSAR Processing

The SBAS InSAR method [11,17] was employed to capture the precursor deformation prior to failure and the subsequent deformation evolution. In this process, COP-DEM and GACOS data [32–34] were utilized to correct terrain-induced phases and suppress atmospheric phase contributions. Considering the uneven data distribution, we established a temporal baseline threshold of 100 days and a spatial baseline threshold of 120 m for pre-failure Sentinel-1 ascending data, 100 days and 240 m for pre-failure Sentinel-1 descending data, and 240 days and 300 m for post-failure Sentinel-1 ascending data. For Fucheng-1 data, these thresholds were set at 60 days and 200 m. These values were determined through multiple tests to ensure that the SBAS network remained fully connected while striking a balance between achieving high accuracy and maintaining computational efficiency. Figure 3 illustrates the final spatiotemporal baseline networks corresponding to the four datasets. To mitigate speckle noise and align azimuth with range resolutions, Sentinel-1 interferograms were multi-looked by a factor of 4 × 1 (range × azimuth). For preserving the high-resolution details of Fucheng-1, no multi-looking was applied (factor of 1 × 1). Coherence thresholds of 0.3 for Sentinel-1 and 0.25 for Fucheng-1, estimated using a 5 × 5 moving window, were chosen to mask unreliable pixels. The phases were subsequently unwrapped using the Minimum Cost Flow (MCF) method [35,36]. The unwrapped interferometric phases were then processed using the SBAS algorithm to reconstruct the line-of-sight (LOS) time series displacement and average displacement velocities.

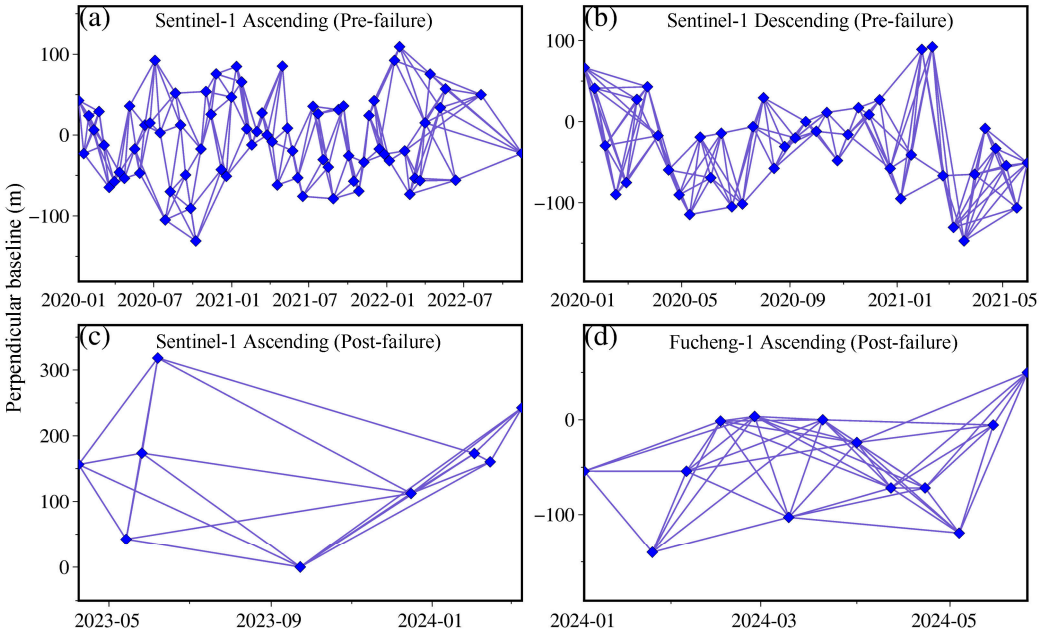

Figure 3. Perpendicular baseline network for four sets of SAR data.

3.3. Horizontal and Vertical Component Decomposition

The LOS velocity (V_{LOS}) is determined by the satellite's viewing geometry and comprises three orthogonal components—V_e, V_n, V_u—corresponding to the east, north, and up directions, respectively, which can be expressed as follows [37,38]:

$$V_{LOS} = \begin{pmatrix} -sin\theta cos\alpha & sin\theta sin\alpha & cos\theta \end{pmatrix} \begin{pmatrix} V_e \\ V_n \\ V_u \end{pmatrix} \quad (1)$$

where θ is the satellite incidence angle, and α represents the satellite orbit heading. To solve for the three unknown orthogonal components, it is typically necessary to combine at least three observation equations or make additional assumptions [23]. The near-north–south orbital heading of SAR satellites renders InSAR largely insensitive to north–south surface motion. As shown in Table 4, only about 10% of possible north–south displacement is captured by the Sentinel-1 and Fucheng-1 InSAR LOS results. Consequently, under the assumption that the contribution of north–south deformation to the LOS results is negligible, Equation (1) can be transformed into:

$$\begin{pmatrix} V_{asc} \\ V_{des} \end{pmatrix} = \begin{pmatrix} -sin\theta_{asc} cos\alpha_{asc} & cos\theta_{asc} \\ -sin\theta_{des} cos\alpha_{des} & cos\theta_{des} \end{pmatrix} \begin{pmatrix} V_e \\ V_u \end{pmatrix} \quad (2)$$

where V_{asc} and V_{des} correspond to LOS velocity vectors for ascending and descending geometries. We combined the LOS results from ascending and descending Sentinel-1 tracks covering the same period to decompose the average vertical and east–west velocities based on Equation (2).

Table 4. Sensitivity of InSAR LOS deformation to north–south motion.

SAR Platform	Orbit	Incidence Angle (°)	Azimuth (°)	Sensitivity *
Sentinel-1	Ascending	37.7	−10.0	10.6%
Sentinel-1	Descending	36.9	−169.9	10.5%
Fucheng-1	Ascending	31.0	−10.2	9.2%

* The sensitivity is defined as the north–south component of the LOS unit vector.

3.4. Pixel Offset Tracking

The POT method essentially measures the relative displacement between two images by estimating their similarity [39,40]. This is achieved through correlation functions—such as Cross Correlation (CC) or Normalized Cross Correlation (NCC)—calculated in either the frequency (Fourier) or spatial domains [41], enabling robust image matching. In this study, we used the frequency-based correlator implemented in the COSI-Corr software [21] to estimate the horizontal deformation of the landslide collapse, utilizing the red band from two PlanetScope images acquired on 22 February 2023 and 24 February 2023 (Table 2). The initial and final window sizes were set to 128 and 32, respectively, to minimize background noise and uncertainties. Search steps of 8 and 4 were tested to explore the trade-off between smoothness and spatial resolution. To further reduce mismatch errors in the image pair, we masked unreliable north–south and east–west displacements with a signal-to-noise ratio (SNR) below 0.9.

3.5. InSAR DEM Generation

In addition to inverting surface deformation signals, another common application of InSAR is the generation of DEM, as exemplified by the well-known SRTM and TanDEM

missions. The equation for reconstructing surface elevation changes using repeat-pass InSAR can be expressed as [42,43]:

$$\Delta h = -\frac{\lambda R sin\theta}{4\pi B_{\perp}} \Delta\varphi_{topo} \tag{3}$$

with measurement accuracy (i.e., standard deviation) expressed by [43,44]:

$$\sigma = \sqrt{\frac{1-\gamma^2}{2\gamma^2}} \cdot \frac{\lambda R sin\theta}{4\pi B_{\perp}} \tag{4}$$

where λ is the wavelength, R represents the distance between the ground and the radar antenna, θ is the incidence angle, $B_{\perp}$ is the perpendicular baseline, φ_{topo} is the topographic phase, and γ is the coherence.

In this study, we used high-resolution SAR images from Fucheng-1 with a short temporal baseline (26 January 2024 and 6 February 2024) to form an interferometric pair for reconstructing the post-failure DEM. The unwrapped interferometric phase (φ) primarily consists of the following components [11]:

$$\varphi = \varphi_{flat} + \varphi_{topo} + \varphi_{defo} + \varphi_{atm} + \varphi_{noi} \tag{5}$$

where the flat-earth phase (φ_{flat}) can be removed using orbital information, and the noise phase (φ_{noi}) can be mitigated through the interferogram filtering method. Given the sufficiently short 11-day revisit interval, a significant surface deformation phase (φ_{defo}) is not expected to have occurred. Under the assumption of negligible atmospheric phase (φ_{atm}), the primary signal observed in the short-time-span interferogram is attributed to elevation changes (φ_{topo}) that have occurred since the generation of the reference DEM used in processing the interferogram [45].

4. Results and Analyses

4.1. Pre-, Co-, and Post-Failure Deformation

Figure 4a,b illustrate the pre-failure deformation of the Xinjing mine area derived from ascending and descending Sentinel-1 tracks, revealing notable deformation across the mining area before the landslide collapse. These deformations primarily cluster on the south slope, where mining activities are concentrated (Figures 1c and 4a,b), and on surrounding disposal sites, largely used for slag dumping (center, northwest, and southeast corners of Dump1, southeast part of Dump2, and the east part of Dump3). The LOS deformation results from ascending and descending tracks exhibit distinct differences in deformation distribution and magnitude, suggesting substantial horizontal displacement. Using the method detailed in Section 3.3, we combined ascending and descending track deformations to retrieve pre-failure vertical and E–W horizontal displacements across the mining area (Figure 5). Results indicate that the south slope experienced subsidence of -50 to -100 mm/yr and eastward movement of 50 to 80 mm/yr, while the southeastern part of the north slope shows subsidence of -20 to -50 mm/yr and a similar rate of westward displacement. This contrasting horizontal movement across the north and south slopes resulted from the SW and NE dip directions of the two slopes. Deformation of the dumps is primarily characterized by pronounced subsidence, with severe deformation zones exhibiting vertical rates of -50 to -80 mm/yr, which may be explained by natural compaction of the slag piles. The landslide area of interest (magenta dashed line in Figures 4a,b and 5) does not show significant anticipated deformation, with only -20 to -30 mm/yr of subsidence and minor eastward movement at the toe of the slope.

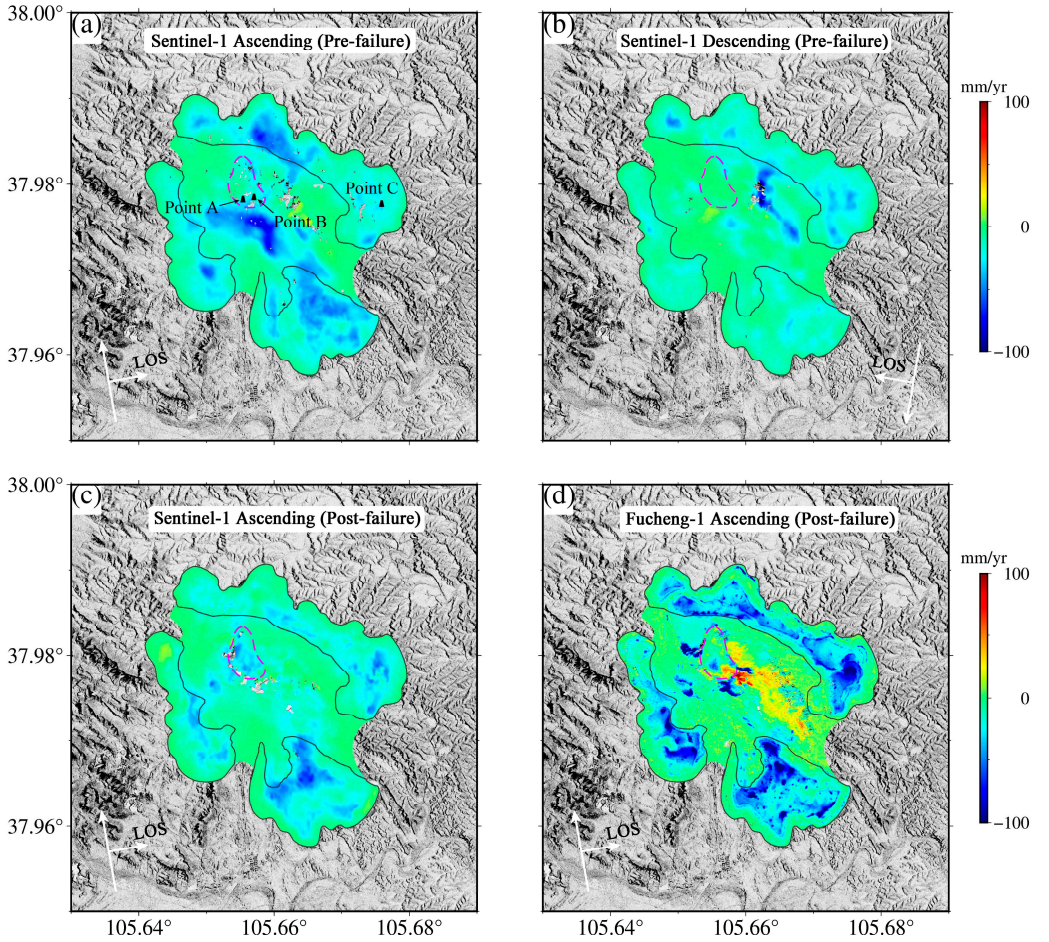

Figure 4. Average LOS deformation velocity of the Xinjing coal mine area derived from (**a**) pre-failure S1-Ascending (20200106–20221115), (**b**) pre-failure S1-Descending (20200111–20210529), (**c**) post-failure S1-Ascending (20230408–20240309), and (**d**) post-failure F1-Ascending data (20240104–20240526). Positive values represent the LOS deformation toward the satellite and negative values the opposite.

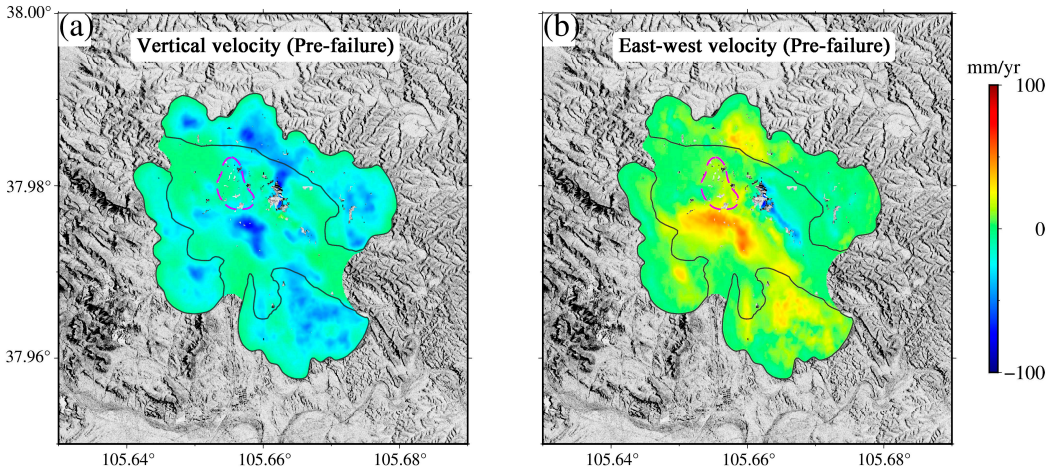

Figure 5. Pre-failure 2D velocity derived from Sentinel-1 ascending and descending tracks. (**a**) Vertical velocity and (**b**) E–W velocity. Positive values represent upward or eastward movement, while negative values indicate the opposite.

Figure 4c,d display the post-failure deformation of the Xinjing mine area as derived from ascending Sentinel-1 and Fucheng-1 satellites, indicating ongoing deformation following the landslide collapse. The LOS rates in the collapse zone from Sentinel-1 (Figure 4c)

increased relative to pre-collapse rates along the same track (Figure 4a), reaching approximately −30 to −50 mm/yr. However, Fucheng-1's ascending post-failure results (Figure 4d) reveal notable differences compared to Sentinel-1, which captured finer deformation details and higher deformation rates. They highlight that post-collapse deformation in the landslide area is primarily concentrated at the slope toe, where localized areas in the east and west of the toe exhibit opposite LOS deformations at rates of approximately 50–70 mm/yr, possibly reflecting the contribution of horizontal components from potential downslope sliding.

To quantitatively assess the accuracy of InSAR monitoring results, we calculated the measurement precision of average velocities (Figure 6) based on the temporal baselines and spatial coherence of the interferograms. Prior to the landslide collapse, the Sentinel-1 ascending (Figure 6a) and descending (Figure 6b) data generally exhibited high accuracy—about 2 mm/yr—across most of the mining area, except in the southeastern part of the north slope, where partial decorrelation reduced accuracy to approximately 7–10 mm/yr. After the collapse, the measurement accuracy of both Sentinel-1 ascending (Figure 6c) and Fucheng-1 ascending (Figure 6d) data deteriorated to roughly 5 mm/yr in most areas, primarily due to the limited number of SAR acquisitions available post-event (Table 1).

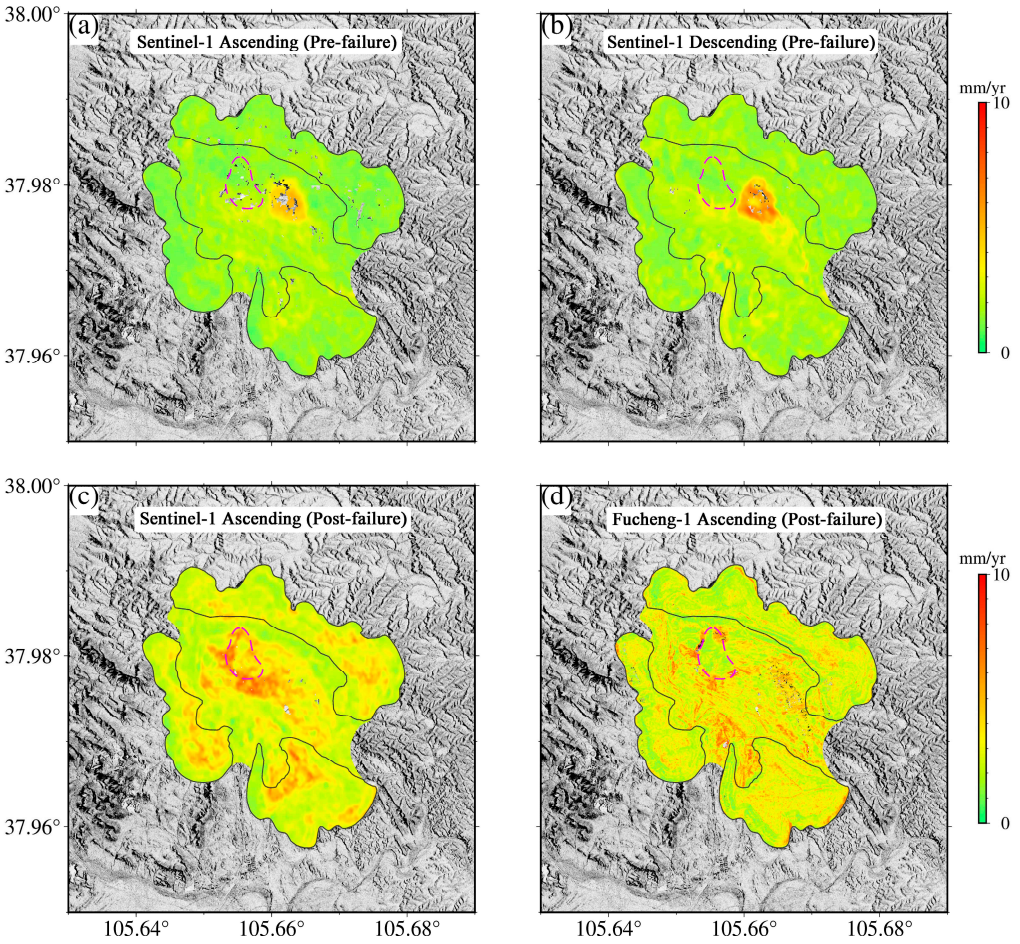

Figure 6. Measurement accuracy (i.e., standard deviation) of InSAR LOS velocities corresponding to Figure 4.

Figure 7 presents the co-failure horizontal deformation retrieved from a PlanetScope image pair acquired the day before and the day after the collapse. We tested search step windows 8 and 4 in the POT processing to explore the trade-off between smoothness and spatial resolution, and the overall results remained consistent. The findings highlight south-

ward displacement of up to 150 m within the collapse area, accompanied by horizontal displacement vectors of approximately 200 m. Although the east–west deformation distribution appears scattered and uneven, the southward displacement is mainly concentrated in the central and lower parts of the landslide (Figure 7a,d).

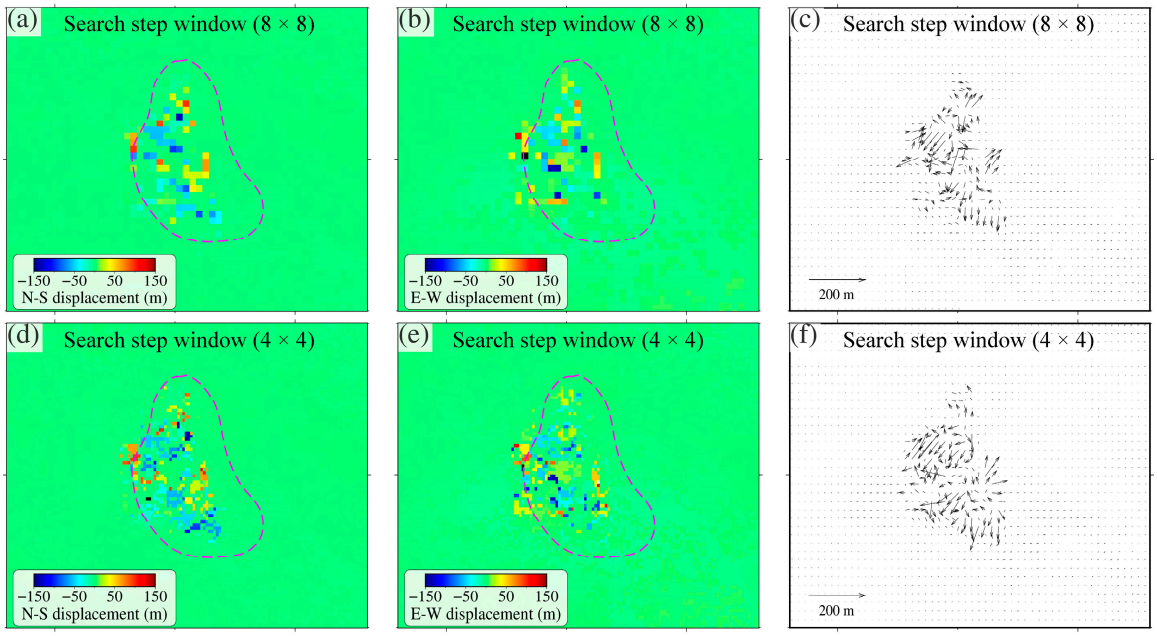

Figure 7. Co-failure deformation derived from POT analysis of PlanetScope images. (**a**,**d**) represent N–S displacement, (**b**,**e**) represent E–W displacement, and (**c**,**f**) indicate horizontal displacement vector. The displacement vectors are average downsampled to 30 m × 30 m grid to mitigate noise.

To investigate the vertical deformation history of the mine area, we reconstructed a post-event DEM using high-resolution Fucheng-1 SAR imagery. We calculated the differences between the InSAR-DEM (2024) and COP-DEM (2011–2015) (Figure 8b), as well as between the COP-DEM and SRTM-DEM (2000) (Figure 8c). The results indicate that deformation between the SRTM-DEM and COP-DEM phases was primarily concentrated on the current south slope, with vertical cumulative deformation ranging from −50 to −130 m. In this phase, deformation in the Dumps was characterized by approximately 50 m of uplift in the central Dump1 and the western Dump3 areas. In contrast, deformation since the COP-DEM phase has mainly occurred on the north slope, where the landslide disaster was located, with larger cumulative changes, reaching −100 to −200 m in the excavation area and approximately 50–120 m of uplift in the Dumps.

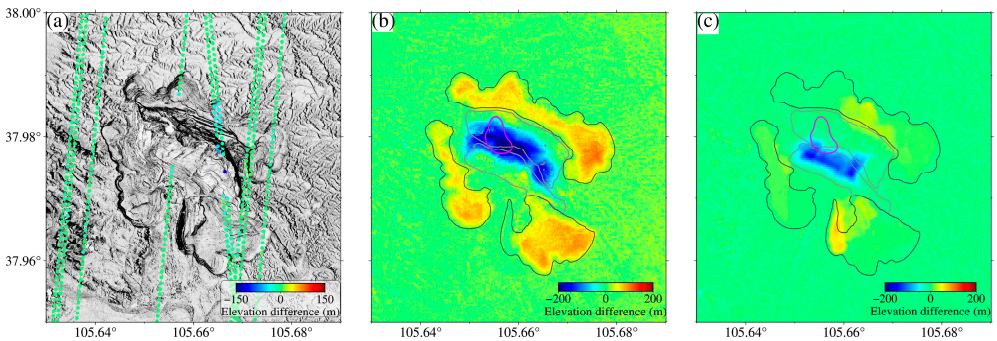

Figure 8. Elevation changes from DEM difference results. (**a**) ICESat-2 elevation minus COP-DEM, (**b**) InSAR-DEM minus COP-DEM, and (**c**) COP-DEM minus SRTM-DEM. Time span of different DEMs is shown in Figure 2 and Table 3.

To verify the accuracy of the InSAR-DEM, we first calculated the theoretical accuracy (i.e., standard deviation) using Equation (4). The results indicate that, apart from the southeastern part of the north slope, the accuracy across most areas of the mining region is better than 10 m (Figure 9a). Additionally, we employed the best fit mid-segment terrain elevation ("h_te_best_fit") from ICESat-2 data (April 2023–November 2023) [31]. We compared the elevation differences between ICESat-2 and COP-DEM (Figure 8a) [46] with those between InSAR-DEM and COP-DEM (Figure 8b). Although ICESat-2 data are sparse in areas with large elevation changes, the available points generally agree well with the InSAR-DEM. Regression analyses and difference histograms between InSAR-DEM and ICESat-2 also indicate good agreement, with an average error of about 16 m (Figure 9).

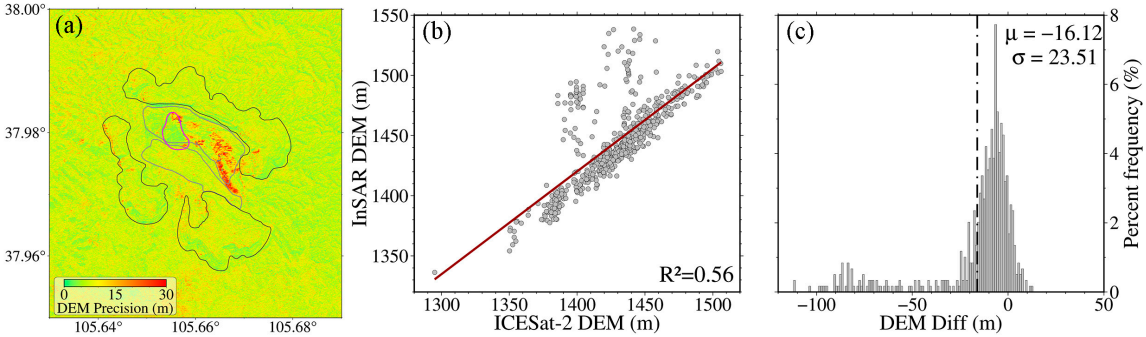

Figure 9. Measurement accuracy of the Fucheng-1 InSAR-DEM. (**a**) Standard deviation values; (**b**) line regression results between InSAR-DEM and ICESat-2 data; (**c**) histogram of differences between InSAR-DEM and ICESat-2 data.

Given the potential surface deformation phase errors in the interferogram used to generate the DEM, we analyzed both incremental and cumulative displacement of the mining area during the Fucheng-1 observation period (Figures S1 and S2). The results indicate that movement between 26 January 2024 and 6 February 2024 was subtle (Figures S1c and S2c), with most areas experiencing less than 5 mm of displacement. Using Equation (3) with $\lambda = 56$ mm, $R = 505$ km, $B_{\perp} = 85.7$ m, and $\theta = 31^{\circ}$, this corresponds to a DEM error of less than 15 m due to potential deformation phase contributions, a magnitude comparable to the differences observed with ICESat-2. Despite variations in accuracy across different DEM datasets, the substantial elevation variations in the mining region (Figure 8b,c) ensure that errors in DEM subtraction have a relatively minor impact, yet still offering valuable insights for assessing elevation changes.

4.2. Time Series Displacement Evloution

To analyze the temporal evolution of deformation, three representative points were selected at the landslide toe and the Dump area to plot cumulative displacement. Notably, points A and B at the slope toe did not show significant deformation before September 2021 (Figure 10a,b), after which accelerated deformation is evident (Figure 10a), especially at point A on the western side, where accelerated deformation persisted until the end of monitoring. Post-collapse, Sentinel-1 results indicate that deformation at points A and B at the toe continues at a slow rate (Figure 10c), while Fucheng-1 shows that point B undergoes reverse movement (Figure 10d). This discrepancy may result from localized downslope sliding toward the southwest, captured by Fucheng-1's higher resolution. In contrast, point C at the Dump area has maintained an approximately constant deformation rate both before and after the collapse.

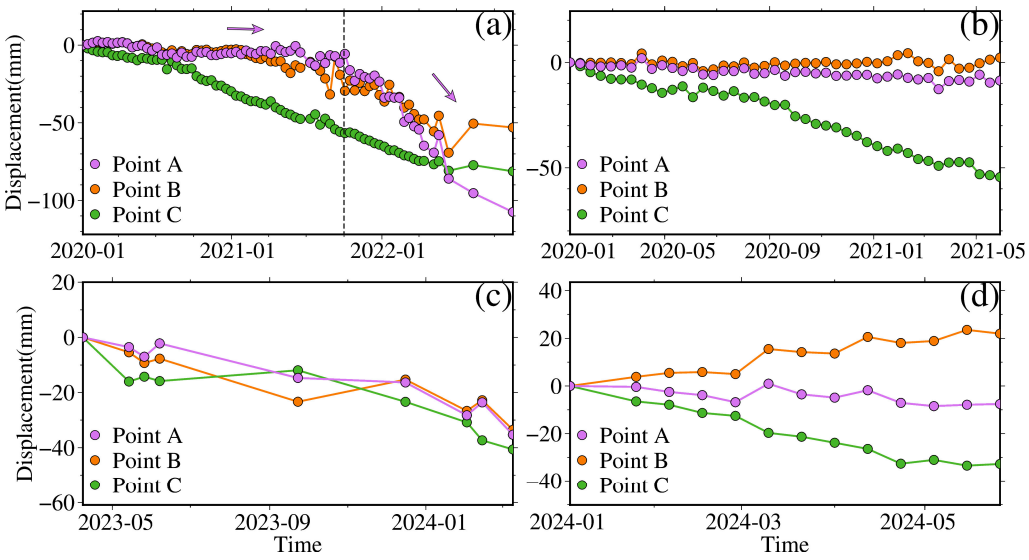

Figure 10. Cumulative LOS displacement of representative points derived from (**a**) pre-failure S1-Ascending, (**b**) pre-failure S1-Descending, (**c**) post-failure S1-Ascending, and (**d**) post-failure F1-Ascending data. The locations of these points are indicated in Figure 4.

5. Discussion

5.1. Underestimation of Sentinel-1 InSAR-Derived Deformation

To investigate the cause of discrepancies between post-failure ascending track monitoring results from Sentinel-1 and Fucheng-1, we conducted multiple parallel SBAS experiments on Fucheng-1 data under different multi-look parameters (Figure 11). Results indicate that as the number of looks increased, the magnitude of deformation gradually decreased. When the range resolution of the two satellites became comparable (Figure 11e,f), the monitoring results from different satellites show good overall consistency, except in some localized areas of the Dumps. Additionally, we selected two profiles crossing the area of intense deformation and plotted the rate variation along these profiles (Figure 12). Results show that with an increasing number of looks, the peak deformation rate gradually decreases, and the deformation distribution becomes smoother and more diffuse. Under the default number of looks (Figure 12b,c,e,f), the peak deformation rates from the two satellites differ by over an order of magnitude.

This discrepancy arises from InSAR's Maximum Detectable Deformation Gradient (MDDG), defined as the maximum detectable displacement over a 1 m ground distance (mm/m). Given the pixel spacing (η) along the slant range (*LOS*) direction and the SAR wavelength (λ), the MDDG in the LOS direction can be represented by [40,47]:

$$MDDG_{los} = \frac{\lambda}{4\eta} \tag{6}$$

When considering arbitrary slope, the *MDDG* along the slope direction can be expressed as [29,48]:

$$MDDG_{slope} = MDDG_{los} \cdot cos\theta \tag{7}$$

where θ denotes the angle between the slope movement direction and the LOS direction.

Considering that both Fucheng-1 and Sentinel-1 operate on the C-band, the theoretical MDDG of Fucheng-1 (1 × 1) is 3.76 times higher than that of Sentinel-1 (1 × 1). When a typical multi-look factor (4 × 1) is applied to Sentinel-1, Fucheng-1's MDDG increases by approximately 15 times.

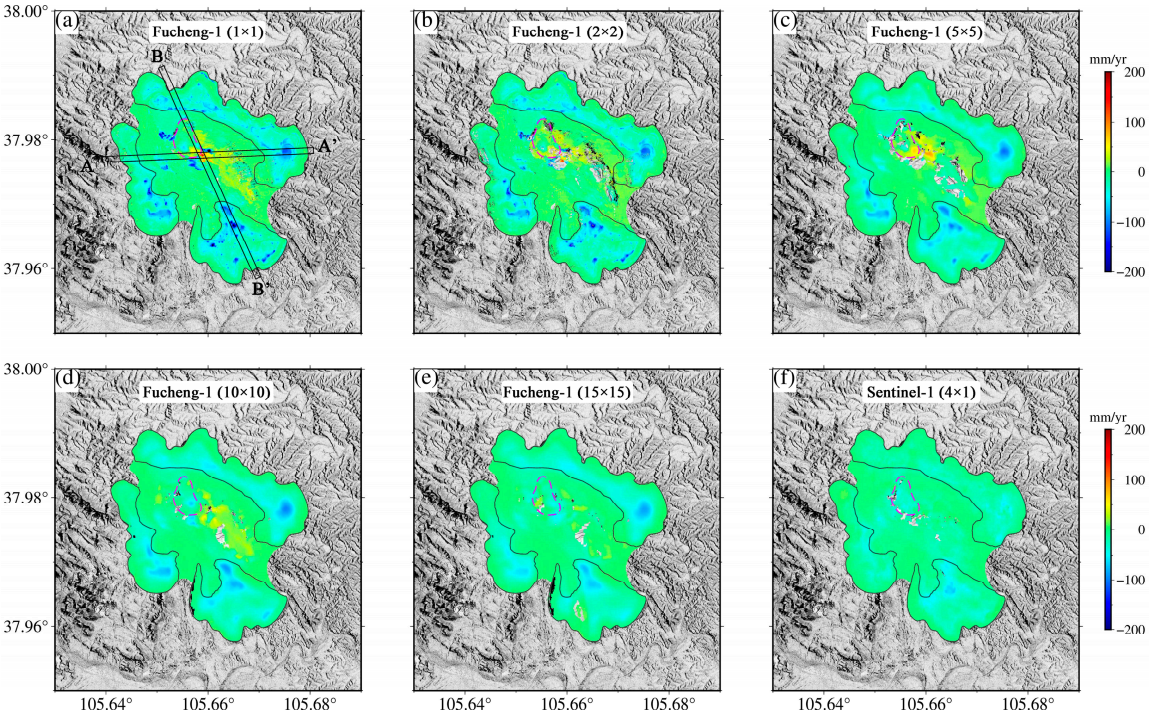

Figure 11. Post-failure ascending LOS velocities for (**a**–**e**) Fucheng-1 and (**f**) Sentinel-1 under different multi-look numbers. The multi-look parameters are labeled within the figures. AA′ and BB′ represent two profiles used for deformation analysis.

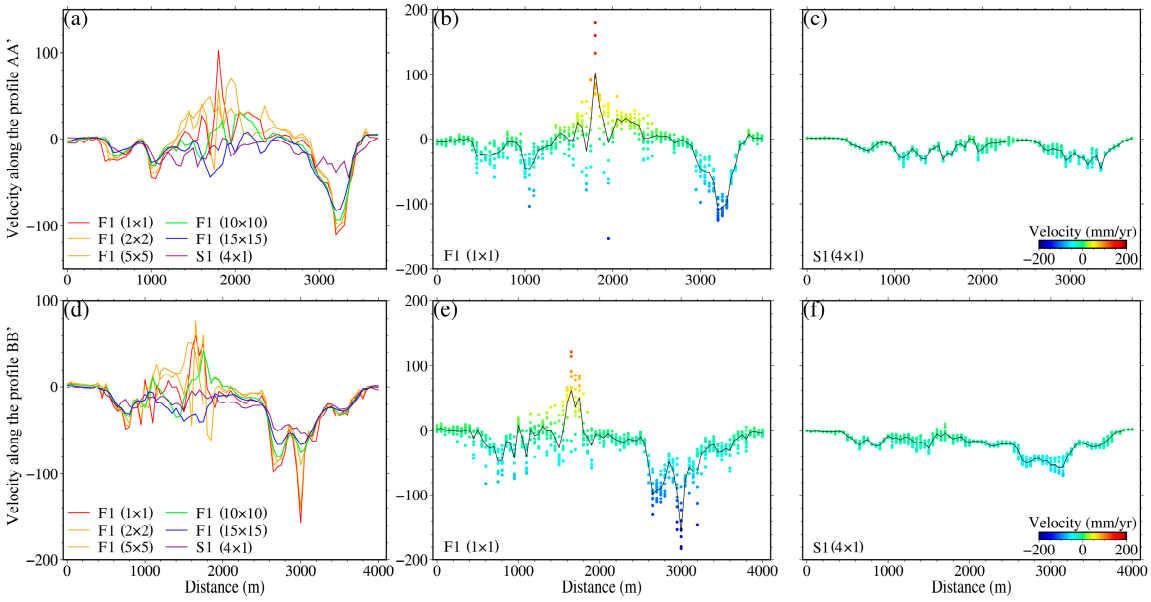

Figure 12. LOS velocity along (**a**–**c**) profile AA′ and (**d**–**f**) BB′ for different multi-look parameters.

It is noteworthy that Equations (6) and (7) represent the theoretical MDDG upper limit assuming a coherence of 1. In practical applications, this theoretical limit decreases rapidly with declining coherence [47]. Fucheng-1's higher coherence under larger multi-look factors results in an actual MDDG superior to that of Sentinel-1, which explains the greater subsidence rates observed in localized Dump areas in Fucheng-1's monitoring results at comparable LOS resolutions (Figure 11e,f).

5.2. Potential Mechanisms for Landslide Failure

The InSAR-derived velocity monitoring results reveal that, prior to the collapse, the landslide's slope toe exhibited deformation rates of approximately 20–30 mm/yr (Figures 4a and 5). The pre-failure deformation time series indicates that significant acceleration in deformation at the slope toe in the landslide area began in September 2021 (Figure 10a), coinciding with the period when the mine underwent technical transformation (transition to open-pit mining) and resumed construction [1,5]. DEM elevation changes also reveal that mining activities in recent years were primarily concentrated on the north slope, especially at the base of the mining area (Figure 8b). According to the accident investigation by the Ministry of Emergency Management of the People's Republic of China, stripping and excavation at the bottom of the stope deepened by 65 m between 2 December 2022 and 19 February 2023 [5]. Such intense stripping and coal mining at the slope toe reduced the resistance against sliding, placing the landslide in an unstable state.

Field investigations also revealed that construction in the mining area deviated significantly from its prescribed design, resulting in an excessively steep and high slope (Figure 13) [4,5]. According to the original design, stripping step heights should not exceed 10 m, with 21 stripping steps and one mining step planned. However, in the actual event area, only three steps were formed, all exceeding 10 m in height, with the tallest reaching 145 m (Figure 13a). The design specified a final stable slope angle of 36°, with a calculated slope stability factor of 4.287, meeting safety standards [5]. However, at the time of the event, the maximum slope height reached 315 m, the overall slope angle increased to 39°, and the local step slope angle reached 61°. The recalculated slope stability factor fell below 1, indicating an unstable condition.

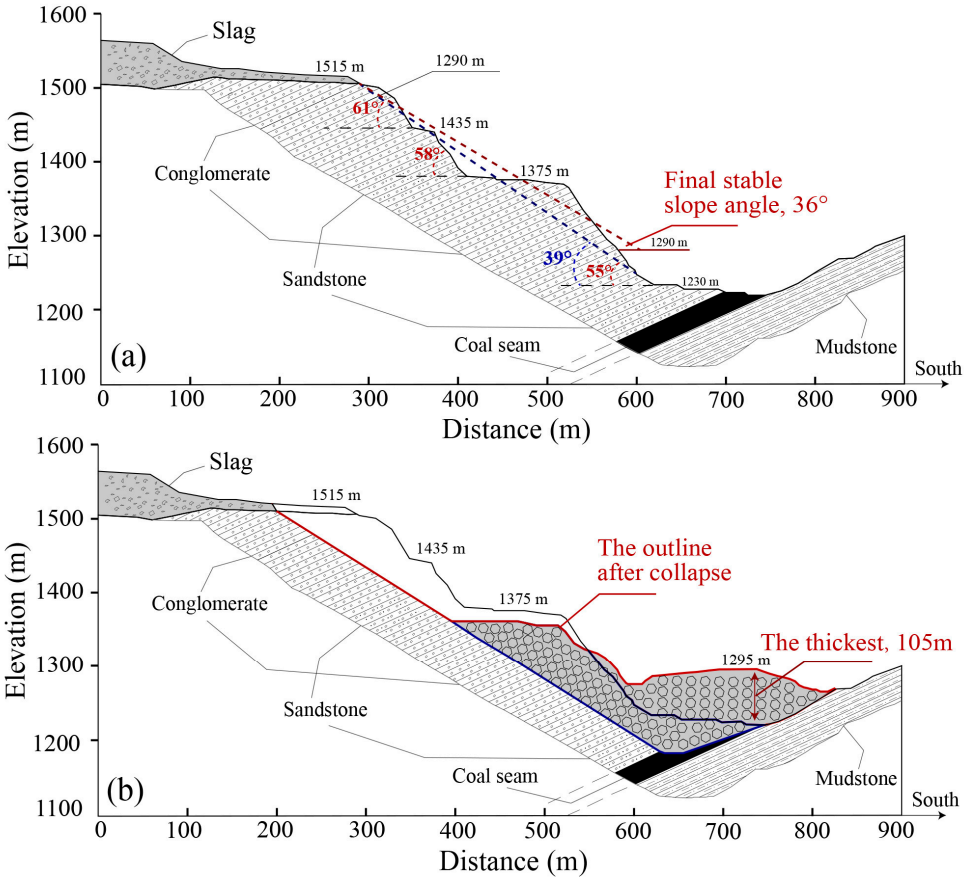

Figure 13. Topographic profile (**a**) before and (**b**) after collapse, revised from [5].

Additionally, slag loading at the top of the landslide also played a role in the collapse (Figure 13). The proximity of the dumping site to the collapse area increased the load on the slope [4]. Continuous disturbances from activities such as stripping and blasting operations likely exacerbated the development of fractures along faults and joint planes within the slope, eventually forming a continuous sliding surface [4,5].

In addition to the primary impact of engineering disturbances, the climatic environment in the study area also played a secondary role. For example, snowfall and subsequent snowmelt within two weeks prior to the collapse may have increased the landslide's gravitational potential and infiltrated the sliding surface, thereby lowering its frictional resistance [2]. During the month preceding the landslide, the average temperature rose steadily above 0 °C, causing repeated freeze–thaw cycles in the near-surface frozen layer [1,4]. This further weakened the geotechnical strength of the near-surface materials and reduced slope stability.

In summary, the combined effect of greater downward force, reduced resisting forces, unfavorable climatic conditions, and the absence of a monitoring and early warning system contributed to this catastrophic event.

5.3. Limitations and Implications

Although we integrated multi-source SAR and optical data to comprehensively capture the full-process deformation of the landslide, this study has the following limitations: (1) Unfortunately, SAR data are not available for the three months preceding the collapse due to a data gap. (2) The limitations in Sentinel-1's MDDG restrict the precise quantification of pre-event deformation, potentially resulting in significant underestimation. (3) Omitting the N–S deformation in deriving 2D vertical and E–W deformations may yield inaccuracies in this region (Table 4), as the NE–SW inclination of the mining slope suggests substantial N–S deformation. (4) Applying POT in the collapse zone poses challenges due to substantial surface texture changes, which may introduce errors. (5) The archived DEM is outdated, lacking real-time DEM data before the event, which hinders accurate quantification of the vertical deformation during the landslide collapse.

The limitations of data availability and MDDG may be mitigated in the future with the increasing deployment of high-resolution mini SAR satellite constellations, such as Fucheng-1 and subsequent satellites in the Mianyang Constellation [29]. Additionally, the limitations of azimuthal deformation monitoring in InSAR may be addressed by the upcoming Harmony (Stereoid) mission [49]. High-resolution DEMs generated from Unoccupied Aircraft System (UAS) or Light Detection and Ranging (LiDAR) measurements may further enable precise quantification of landslide collapse deformation [50,51].

6. Conclusions

In this study, we collected SAR and optical data spanning the catastrophic Xinjing landslide event on 22 February 2023, including Fucheng-1 and Sentinel-1, as well as high-resolution PlanetScope and GF-2 imagery, to elucidate the full-process deformation during the pre-, co-, and post-collapse phases of the landslide. The results reveal that pre-failure deformation was primarily concentrated at the slope toe, with a notable acceleration in deformation beginning in September 2021, highlighting the potential hazard. During the collapse, the main movement of the landslide was characterized by a southward displacement of approximately 150 m, with a maximum horizontal displacement of about 200 m. Post-collapse, localized deformation continues at the slope toe, emphasizing the contribution of potential downslope movement's horizontal component. Combining these deformation results with previous field investigation data, we conclude that the collapse was primarily triggered by continuous excavation at the slope's base and excessively steep, non-compliant artificial slope design.

Due to the limitations of MDDG, significant differences in post-failure deformation monitoring results between Sentinel-1 and Fucheng-1 are observed. Under the default multi-look parameters in this experiment (1 × 1 for Fucheng-1 and 4 × 1 for Sentinel-1), the MDDG of Fucheng-1 is approximately 15 times higher due to its higher spatial resolution, thus capturing larger deformation rate peaks and finer deformation details. This implies that even when monitoring pre- and post-failure continuous deformation of landslides in mining areas, Sentinel-1 InSAR may significantly underestimate the deformation. This underscores the necessity of checking MDDG in advance when using time series InSAR to monitor regions experiencing rapid surface changes.

In the context of rapidly advancing remote sensing technologies, particularly the increasing deployment of multi-platform SAR satellites, remote-sensing-based real-time monitoring of mining-induced landslides offers unparalleled advantages, such as extensive spatial coverage and comprehensive observations. This approach provides critical Supplementary Information to in situ monitoring methods and holds the potential to become an essential early warning tool, thereby helping to prevent similar catastrophic events.

Supplementary Materials: The following supporting information can be downloaded at: https://www.mdpi.com/article/10.3390/rs17010019/s1, Figure S1: Incremental LOS displacement maps derived from Fucheng-1 ascending data; Figure S2: Cumulative LOS displacement maps derived from Fucheng-1 ascending data.

Author Contributions: Conceptualization, F.C. and S.D.; methodology, F.C. and H.L.; software, H.L.; validation, F.C., S.D. and H.Y.; formal analysis, F.C. and H.L.; investigation, F.C. and H.L.; resources, S.D. and H.Y.; data curation, F.C. and H.L.; writing—original draft preparation, F.C.; writing—review and editing, F.C., H.L, S.D. and H.Y.; visualization, F.C. and H.L.; supervision, S.D.; project administration, S.D.; funding acquisition, S.D. and H.Y. All authors have read and agreed to the published version of the manuscript.

Funding: This research was supported by the National Natural Science Foundation of China (Nos. 42072320, 41972219, and 42372264).

Data Availability Statement: The Fucheng-1 SAR data are restricted from public sharing in this article due to privacy considerations. Sentinel-1 SAR data are openly accessible through the Alaska Satellite Facility (https://search.asf.alaska.edu, accessed on 22 July 2024), and ICEsat-2 data can be freely accessed from the National Snow and Ice Data Center (https://nsidc.org/data/icesat-2, accessed on 24 July 2024). GACOS data are openly accessible from http://www.gacos.net/ (accessed on 28 July 2024).

Acknowledgments: We gratefully acknowledge Spacety Co., Ltd. for providing Fucheng-1 SAR images and Planet Labs Company for granting access to PlanetScope data under an education and research license. Pixel offset tracking of optical images was conducted using COSI-Corr (http://www.tectonics.caltech.edu/slip_history/spot_coseis/download_software.html, accessed on 28 July 2024). ICEsat-2 data are copyrighted by the National Aeronautics and Space Administration (NASA) of the United States. Some figures were generated with GMT.

Conflicts of Interest: The authors declare no conflicts of interest.

References

1. Zhang, N.; Wang, Y.; Zhao, F.; Wang, T.; Zhang, K.; Fan, H.; Zhou, D.; Zhang, L.; Yan, S.; Diao, X. Monitoring and Analysis of the Collapse at Xinjing Open-Pit Mine, Inner Mongolia, China, Using Multi-Source Remote Sensing. *Remote Sens.* **2024**, *16*, 993. [CrossRef]
2. An, B.; Wang, C.; Liu, C.; Li, P. A multi-source remote sensing satellite view of the February 22nd Xinjing landslide in the mining area of Alxa left Banner, China. *Landslides* **2023**, *20*, 2517–2523. [CrossRef]
3. Li, H.; She, C.; Zhou, Y.; Huang, Y. Summary and prospect of open-pit coal mining technology in China. *Coal Sci. Technol.* **2019**, *47*, 24–35.

4. Wang, Q.; Xing, A.; Xu, X.; Zhou, Y.; Yang, Q.; Song, H.; Peng, J.; Zhai, L.; Bilal, M.; Liu, Y. Formation mechanism and dynamic process of open-pit coal mine landslides: A case study of the Xinjing landslide in Inner Mongolia, China. *Landslides* **2024**, *21*, 541–556. [CrossRef]
5. Ministry of Emergency Management of the People's Republic of China. Available online: https://www.mem.gov.cn (accessed on 28 August 2024).
6. Li, Z.; Li, W.; Xu, Q.; Lu, H.; Fu, H.; Guo, P.; Zhao, J.; Yu, C. Preliminary analysis of the catastrophic February 22nd 2023 Xinjing open-pit mine landslide, Inner Mongolia, China. *Landslides* **2024**, *21*, 1053–1067. [CrossRef]
7. Dick, G.J.; Eberhardt, E.; Cabrejo-Liévano, A.G.; Stead, D.; Rose, N.D. Development of an early-warning time-of-failure analysis methodology for open-pit mine slopes utilizing ground-based slope stability radar monitoring data. *Can. Geotech. J.* **2015**, *52*, 515–529. [CrossRef]
8. Ye, X.; Zhu, H.; Wang, J.; Zheng, W.; Zhang, W.; Schenato, L.; Pasuto, A.; Catani, F. Towards hydrometeorological thresholds of reservoir-induced landslide from subsurface strain observations. *Sci. China-Technol. Sci.* **2024**, *67*, 1907–1922. [CrossRef]
9. Liu, S.; Wu, L.; Mao, Y.; He, L.; Wang, Z.; Xu, Z.; Wei, L.; Yang, Z. Spaceborne-airborne-ground collaborated intelligent monitoring on open-pit slope and its typical applications. *J. China Coal Soc.* **2020**, *45*, 2265–2276. [CrossRef]
10. Lian, X.; Li, Z.; Yuan, H.; Hu, H.; Cai, Y.; Liu, X. Determination of the stability of high-steep slopes by global navigation satellite system (GNSS) real-time monitoring in long wall mining. *Appl. Sci.* **2020**, *10*, 1952. [CrossRef]
11. Chang, F.; Dong, S.; Yin, H.; Wu, Z. Using the SBAS InSAR technique to monitor surface deformation in the Kuqa fold-thrust belt, Tarim Basin, NW China. *J. Asian Earth Sci.* **2022**, *231*, 105212. [CrossRef]
12. Ye, X.; Kaufmann, H.; Guo, X. Landslide monitoring in the Three Gorges area using D-InSAR and corner reflectors. *Photogramm. Eng. Remote Sens.* **2004**, *70*, 1167–1172. [CrossRef]
13. Hooper, A.; Zebker, H.; Segall, P.; Kampes, B. A new method for measuring deformation on volcanoes and other natural terrains using InSAR persistent scatterers. *Geophys. Res. Lett.* **2004**, *31*, L23611. [CrossRef]
14. Hooper, A. A multi-temporal InSAR method incorporating both persistent scatterer and small baseline approaches. *Geophys. Res. Lett.* **2008**, *35*, L16302. [CrossRef]
15. Ferretti, A.; Prati, C.; Rocca, F. Permanent scatterers in SAR interferometry. *IEEE Trans. Geosci. Remote Sens.* **2001**, *39*, 8–20. [CrossRef]
16. Ferretti, A.; Novali, F.; Bürgmann, R.; Hilley, G.; Prati, C. InSAR permanent scatterer analysis reveals ups and downs in San Francisco Bay area. *Eos* **2004**, *85*, 317–324. [CrossRef]
17. Berardino, P.; Fornaro, G.; Lanari, R.; Sansosti, E. A new algorithm for surface deformation monitoring based on small baseline differential SAR interferograms. *IEEE Trans. Geosci. Remote Sens.* **2002**, *40*, 2375–2383. [CrossRef]
18. Chang, F.; Dong, S.; Yin, H.; Ye, X.; Wu, Z.; Zhang, W.; Zhu, H. Unravelling long-term spatiotemporal deformation and hydrological triggers of slow-moving reservoir landslides with multi-platform SAR data. *Int. J. Appl. Earth Obs. Geoinf.* **2024**, *135*, 104301. [CrossRef]
19. Hooper, A.; Bekaert, D.; Spaans, K.; Arıkan, M. Recent advances in SAR interferometry time series analysis for measuring crustal deformation. *Tectonophysics* **2012**, *514–517*, 1–13. [CrossRef]
20. Singleton, A.; Li, Z.; Hoey, T.; Muller, J.-P. Evaluating sub-pixel offset techniques as an alternative to D-InSAR for monitoring episodic landslide movements in vegetated terrain. *Remote Sens. Environ.* **2014**, *147*, 133–144. [CrossRef]
21. Leprince, S.; Barbot, S.; Ayoub, F.; Avouac, J.-P. Automatic and precise orthorectification, coregistration, and subpixel correlation of satellite images, application to ground deformation measurements. *IEEE Trans. Geosci. Remote Sens.* **2007**, *45*, 1529–1558. [CrossRef]
22. Samsonov, S.; Tiampo, K.; Cassotto, R. SAR-derived flow velocity and its link to glacier surface elevation change and mass balance. *Remote Sens. Environ.* **2021**, *258*, 112343. [CrossRef]
23. Chang, F.; Dong, S.; Yin, H.; Ye, X.; Zhang, W.; Zhu, H.-H. Temporal stacking of sub-pixel offset tracking for monitoring slow-moving landslides in vegetated terrain. *Landslides* **2024**, *21*, 1255–1271. [CrossRef]
24. Hu, X.; Lu, Z.; Pierson, T.C.; Kramer, R.; George, D.L. Combining InSAR and GPS to Determine Transient Movement and Thickness of a Seasonally Active Low-Gradient Translational Landslide. *Geophys. Res. Lett.* **2018**, *45*, 1453–1462. [CrossRef]
25. An, P.; Yong, R.; Wang, C.; Jia, S.; Fang, K. Utilizing crowdsourced data for timely investigation of catastrophic landslide accidents: A case study of the coal mine collapse in inner Mongolia, China. *Bull. Eng. Geol. Environ.* **2024**, *83*, 354. [CrossRef]
26. Wu, H.; Zhang, Y.; Kang, Y.; Wei, J.; Liu, Y.; Li, B. Fine mapping of surface deformation in Xinjing open-pit mine, Inner Mongolia using FS-InSAR technique. *Geomat. Inf. Sci. Wuhan Univ.* **2024**, *49*, 389–399. [CrossRef]
27. Deng, Q.; Liao, Y. Paleoseismology along the range-front fault of Helan Mountains, north central China. *J. Geophys. Res. Solid Earth* **1996**, *101*, 5873–5893. [CrossRef]
28. Spacety Co., Ltd. Available online: https://cn.spacety.com/ (accessed on 28 June 2024).
29. Feng, S.; Dai, K.; Sun, T.; Deng, J.; Tang, G.; Han, Y.; Ren, W.; Sang, X.; Zhang, C.; Wang, H. Mini-Satellite Fucheng 1 SAR: Interferometry to Monitor Mining-Induced Subsidence and Comparative Analysis with Sentinel-1. *Remote Sens.* **2024**, *16*, 3457. [CrossRef]

30. Planet Team. Planet Application Program Interface: In Space for Life on Earth. San Francisco, CA. Available online: https://www.planet.com/ (accessed on 1 March 2023).
31. Neuenschwander, A.L.; Pitts, K.L.; Jelley, B.P.; Robbins, J.; Markel, J.; Popescu, S.C.; Nelson, R.F.; Harding, D.; Pederson, D.; Klotz, B.; et al. ATLAS/ICESat-2 L3A Land and Vegetation Height. (ATL08, Version 6). 2023. Available online: https://nsidc.org/data/atl08/versions/6 (accessed on 24 July 2024).
32. Yu, C.; Li, Z.; Penna, N.T.; Crippa, P. Generic atmospheric correction model for interferometric synthetic aperture radar observations. *J. Geophys. Res. Solid Earth* **2018**, *123*, 9202–9222. [CrossRef]
33. Yu, C.; Li, Z.; Penna, N.T. Interferometric synthetic aperture radar atmospheric correction using a GPS-based iterative tropospheric decomposition model. *Remote Sens. Environ.* **2018**, *204*, 109–121. [CrossRef]
34. Yu, C.; Penna, N.T.; Li, Z. Generation of real-time mode high-resolution water vapor fields from GPS observations. *J. Geophys. Res.-Atmos.* **2017**, *122*, 2008–2025. [CrossRef]
35. Pepe, A.; Lanari, R. On the extension of the minimum cost flow algorithm for phase unwrapping of multitemporal differential SAR interferograms. *IEEE Trans. Geosci. Remote Sens.* **2006**, *44*, 2374–2383. [CrossRef]
36. Costantini, M. A novel phase unwrapping method based on network programming. *IEEE Trans. Geosci. Remote Sens.* **1998**, *36*, 813–821. [CrossRef]
37. Fuhrmann, T.; Garthwaite, M.C. Resolving three-dimensional surface motion with InSAR: Constraints from multi-geometry data fusion. *Remote Sens.* **2019**, *11*, 241. [CrossRef]
38. Chang, F.; Dong, S.; Yin, H.; Wu, Z.; Wang, W. Kinematic Response of Subaerial Salt Diapirs to Geomorphic, Tectonic and Climatic Regimes: Insights From Space-Based Observations in the Western Kuqa Fold-Thrust Belt, NW China. *Tectonics* **2023**, *42*, e2022TC007670. [CrossRef]
39. Provost, F.; Michéa, D.; Malet, J.-P.; Boissier, E.; Pointal, E.; Stumpf, A.; Pacini, F.; Doin, M.-P.; Lacroix, P.; Proy, C. Terrain deformation measurements from optical satellite imagery: The MPIC-OPT processing services for geohazards monitoring. *Remote Sens. Environ.* **2022**, *274*, 112949. [CrossRef]
40. Sun, L.; Muller, J.-P. Evaluation of the use of sub-pixel offset tracking techniques to monitor landslides in densely vegetated steeply sloped areas. *Remote Sens.* **2016**, *8*, 659. [CrossRef]
41. Heid, T.; Kääb, A. Evaluation of existing image matching methods for deriving glacier surface displacements globally from optical satellite imagery. *Remote Sens. Environ.* **2012**, *118*, 339–355. [CrossRef]
42. Yu, J.H.; Ge, L.; Rizos, C. Digital elevation model generation using multibaseline advanced land observing satellite/phased array type L-band synthetic aperture radar imagery. *J. Appl. Rem. Sens.* **2011**, *5*, 053510. [CrossRef]
43. Hanssen, R.F. *Radar Interferometry: Data Interpretation and Error Analysis*; Springer Science & Business Media: Berlin/Heidelberg, Germany, 2001; Volume 2.
44. Rosen, P.A.; Hensley, S.; Joughin, I.R.; Li, F.K.; Madsen, S.N.; Rodriguez, E.; Goldstein, R.M. Synthetic aperture radar interferometry. *Proc. IEEE* **2000**, *88*, 333–382. [CrossRef]
45. Prush, V.B.; Lohman, R.B. Time-varying elevation change at the centralia coal mine in centralia, Washington (USA), constrained with InSAR, ASTER, and optical imagery. *IEEE J. Sel. Top. Appl. Earth Observ. Remote Sens.* **2014**, *8*, 919–925. [CrossRef]
46. Lou, J.; Zhao, C.; Li, G.; Li, D. Inversion of Time series Elevation Changes in Open Pit Mining Areas Based on Adjacent Orbital Sentinel-2 Images. *IEEE J. Sel. Top. Appl. Earth Observ. Remote Sens.* **2024**, *17*, 6126–6133. [CrossRef]
47. Jiang, M.; Li, Z.; Ding, X.; Zhu, J.; Feng, G. Modeling minimum and maximum detectable deformation gradients of interferometric SAR measurements. *Int. J. Appl. Earth Obs. Geoinf.* **2011**, *13*, 766–777. [CrossRef]
48. Dai, K.; Chen, Y.; Xu, Q.; Hancock, C.; Jiang, M.; Deng, J.; Zhuo, G. A functional model for determining maximum detectable deformation gradients of InSAR considering the topography in mountainous areas. *IEEE Trans. Geosci. Remote Sens.* **2023**, *61*, 1–11. [CrossRef]
49. Li, Y.; Lopez-Dekker, P.; Iannini, L.; Prats-Iraola, P. Performance of 2-D deformation measurements by the multi-static harmony (Stereoid) mission. In Proceedings of the IGARSS 2019—2019 IEEE International Geoscience and Remote Sensing Symposium, Yokohama, Japan, 28 July–2 August 2019; pp. 8826–8829.
50. Dille, A.; Kervyn, F.; Handwerger, A.L.; d'Oreye, N.; Derauw, D.; Bibentyo, T.M.; Samsonov, S.; Malet, J.-P.; Kervyn, M.; Dewitte, O. When image correlation is needed: Unravelling the complex dynamics of a slow-moving landslide in the tropics with dense radar and optical time series. *Remote Sens. Environ.* **2021**, *258*, 112402. [CrossRef]
51. Xu, Y.; Lu, Z.; Schulz, W.; Kim, J. Twelve-year dynamics and rainfall thresholds for alternating creep and rapid movement of the Hooskanaden landslide from integrating InSAR, pixel offset tracking, and borehole and hydrological measurements. *J. Geophys. Res. Earth Surf.* **2020**, *125*, e2020JF005640. [CrossRef]

Disclaimer/Publisher's Note: The statements, opinions and data contained in all publications are solely those of the individual author(s) and contributor(s) and not of MDPI and/or the editor(s). MDPI and/or the editor(s) disclaim responsibility for any injury to people or property resulting from any ideas, methods, instructions or products referred to in the content.